Korean J. Chem. Eng., 39(7), 1959-1967 (2022)
DOI: 10.1007/s11814-021-1003-1

pISSN: 0256-1115
eISSN: 1975-7220

Hierarchical multi-metal-doped mesoporous NiO-silica nanoparticles towards a viable platform for Li-ion battery electrode application

Nabanita Pal*, Jae Won Jo, Daulatabad Narsimulu***, Eun-Bum Cho**,†, and Jae Su Yu***,†**

*Department of Physics and Chemistry, Mahatma Gandhi Institute of Technology, Gandipet, Hyderabad 500075, India
**Department of Fine Chemistry, Seoul National University of Science and Technology, Seoul 01811, Korea
***Department of Electronics and Information Convergence Engineering, Institute for Wearable Convergence Electronics, Kyung Hee University, 1732 Deogyeong-daero, Gihung-gu, Yongin-si, Gyeonggi-do 17104, Korea
(*Received 15 September 2021 • Revised 19 October 2021 • Accepted 2 November 2021*)

Abstract−Hierarchical nanostructures have received wide attention for their distinguished physical and chemical properties of the synthesized materials, mainly in future energy storage applications. In this study, Ni-based multi-metal doped silica mesoporous nanoflowers were prepared and characterized as a potential anode material for lithium ion batteries. A facile synthesis strategy is depicted here for Ni-based multi-metal doped silica mesoporous nanoflowers by using a CTAB surfactant and ammonia basic media in water-ethanol mixed solvent media. Ce, Al, Mn, and Co species have been chosen as other additive metals for doping in this mesostructure in order to find the enhanced electrochemical performance of the Ni-based silica. Systematic characterization of the material was performed by transmission electron microscopy (TEM), scanning electron microscopy (SEM), wide-angle X-ray diffraction (WA-XRD) analysis and N_2 sorption, which show 500-600 nm sized particles with fine-looking nanoflower morphology and surface area in the range of 211-405 m^2g^{-1}. The initial charge/discharge capacity was found to be 1,313/178, 990/436, 1,122/234 and 1,585/689 mA h g^{-1} for different Ni-silica, Ni-Ce-silica, Ni-Al-silica and Ni-Co-Mn-Al-silica electrodes, respectively. The enhanced electrochemical performance for Ce doped Ni-silica compared to other mesoporous samples may be attributed to improved electrical conductivity as well as the hierarchical nanoflower-like structure.

Keywords: Multi-metal Mesoporous Silica, Ni-based Composite Oxide, Nanoparticle, Electrochemical Property, Li-ion Battery

INTRODUCTION

In 21st century, rapid economic growth, unlimited industrial development, excessive use of fossil fuel and increasing human population have led to a serious alteration of the global environment, which has become a matter of concern [1]. To ensure true sustainability for future generations and for the protection of earth's environment, there is a worldwide search for alternative renewable energy resources that are non-polluting, eco-friendly, as well as has high efficiency to fulfill the energy demand [2]. Along with highly trending renewable resources like solar power and wind energy [3,4], high performance rechargeable Li-ion batteries (LIBs) also have gained worldwide recognition as an efficient and long-term energy conversion and storage device for electric vehicles and grid applications [5,6]. Thus, much effort has been devoted to developing more advanced and high-performing, next-generation Li-ion batteries. These could be the most advantageous secondary batteries with high specific energy and energy density, long cycle life as well as a significantly safe and environment friendly energy storage devices [5-8].

Relatively low theoretical capacity (~372 mA h g^{-1}), reduced rate performance and safety issues are some of the main drawbacks of graphite anode, commonly used in LIBs, which limits its application for high-energy storage purposes [9]. Hence, transition metals like Co, Ni, Mn, Fe, and V-based oxides and mixed oxides have become quite popular as an electrode material for LIB owing to their low cost, high specific theoretical capacity (~600-1,000 mA h g^{-1}) and abundance in the earth's crust [10-12]. On the other hand, non-toxicity, high specific surface area, porous structure, low bulk density of SiO_2 nanomaterials make it an essential candidate for LIBs facilitating Li-ion mass transportation, improving mechanical stability and reaction rate [13]. However, due to low thermal and electrical conductivity, the performance of pristine SiO_2 is not satisfactory [14], so proper tuning of silica structure with significant loading of transition metals or metal oxides can improve the electrochemical capability of the parent material. Ni has been proved highly efficient as electrode material in LIBs. Although there are many reports regarding the significant electrical performance based on Ni-based materials [15,16], very few reports have been published on the Li-ion battery energy applications of porous oxide-silica composite materials. In the present study, we describe a facile route for synthesis of some 3D hierarchical nanoflower structured multi-metal-doped (i.e., Ce, Al, Mn, Co) porous nickel-silica nanocomposites which have shown good electrical performance as anode materials for Li-ion battery. Among various morphology-controlled nanoparticles, nanoflower is a new class of morphology with 3D hierarchical structure which shows a significant potential in catalysis [17], biosensors [18], drug delivery [19], energy

†To whom correspondence should be addressed.
E-mail: echo@seoultech.ac.kr, jsyu@khu.ac.kr

Table 1. Nomenclature and the experimental parameters for all Ni-based multimetal doped silica microspheres

Sample	CTAB (g)	H_2O (mL)	Ethanol (mL)	NH_4OH (mL)	TEOS (mL)	$Ce(OH)_4$ (g)	$AlCl_3$ $6H_2O$ (g)	$Mn(CH_3CO_2)_2$ $4H_2O$ (g)	$Co(NO_3)_2$ $6H_2O$ (g)	$Ni(NO_3)_2$ $6H_2O$ (g)
NS	3.0	60	91.2	70	3.0	0	0	0	0	11.72
NCeS	3.0	60	91.2	70	6.0	3.36	0	0	0	4.68
NAS	3.0	60	91.2	70	6.0	0	3.88	0	0	4.70
NCMAS	3.0	60	91.2	70	6.0	0	1.30	1.30	1.36	7.84

applications [20] and other promising research fields owing to its high surface to volume ratio, higher surface area, better charge transfer capacity, facile synthesis method and so on [21]. Recently, numerous binary and ternary metal oxides with nanoflower architectures have been reported as exceptionally effective anode materials for Li-ion batteries [22,23]. Even, metal oxide nanoflowers supported on reduced graphene oxide (r-GO) [24] or carbon nanotubes (CNT) [25] have proven quite efficient in next-generation rechargeable LIB application. However, till now, Li-ion battery performance over oxide-silica nanoflower composites has not been explored properly.

Hence, our present study has three major directions: 1) finding a simple sol-gel hydrothermal route for the generation of multimetal doped nickel-silica 3D hierarchical porous nanoflower structures, 2) evaluation of its energy application as an anode material for Li-ion battery, which is one of the important alternatives for future energy demand, and 3) investigation of the change in electrochemical performance of nickel-silica nanocomposites and the effect on morphology, properties by doping multiple metals selected from *p*-block, *d*-block and *f*-block of the periodic table like Al, Co, Mn, Ce, respectively.

EXPERIMENTAL

1. Materials

For the preparation of Ni-based multi-metal doped silica samples nickel(II) nitrate hexahydrate ($Ni(NO_3)_2{\cdot}6H_2O$, Aldrich), cerium (IV) hydroxide ($Ce(OH)_4$, Aldrich), aluminium(III) chloride hexahydrate ($AlCl_3{\cdot}6H_2O$, Aldrich), manganese acetate tetrahydrate ($Mn(CH_3COO)_2{\cdot}4H_2O$, Aldrich), cobalt(II) nitrate hexahydrate ($Co(NO_3)_2{\cdot}6H_2O$, Aldrich) were used as Ni, Ce, Al, Mn, Co precursors, respectively. Tetraethyl orthosilicate (TEOS, 98%, Aldrich) was used as a silica precursor. Structure-directing agent CTAB or hexadecyltrimethylammonium bromide (98%) was purchased from Aldrich. Both ammonium hydroxide (NH_4OH, 28-30% NH_3) and ethanol (EtOH) were obtained from Aldrich. EtOH acted as a co-solvent during the multi-metal doped silica synthesis, whereas NH_4OH was used to maintain the basic media. Deionized water prepared in our laboratory was used as a main solvent for the sol-gel reaction. All the chemicals were used without further purification.

2. Synthesis Procedure for Ni-based Multi-metal Doped Silica

Cationic surfactant CTAB and NH_4OH basic media were applied for the preparation of Ni-based multi-metal doped silica samples. In a typical synthesis for pure Ni-based silica material (named as NS), 3.0 g (8.2 mmol) of CTAB was dissolved in 60 mL of deionized water and 91.2 mL of ethanol under vigorous stirring at normal temperature in a glass bottle. Next 70 mL (1.0 mol) of ammonia solution was added gradually into the CTAB-water-ethanol mixture. After continuous stirring of more than 30 min, 3 mL (13.4 mmol) of TEOS was added to it and the mixture was kept under stirring condition for another exact 30 min. A heavy white precipitate formed gradually in the mixture. Next, 11.72 g (42.98 mmol) of $Ni(NO_3)_2{\cdot}6H_2O$ was added slowly to this and the final mixture was constantly stirred for 24 h at room temperature. Then a hydrothermal treatment was done with this mixture in a convection oven at 373 K for 24 h. Finally, the mixture was cooled, filtered followed by washing with deionized water and ethanol. To remove the surfactant, first the sample was dried in air and then calcined at 823 K for 5 h at atmospheric condition.

A similar method was applied for the syntheses of other samples (named as NCeS, NAS and NCMAS) by adding Ce precursor, Al precursor and a mixture of Al, Mn, Co precursors, respectively, into the above-mentioned Ni-Silica based CTAB-ethanol-water mixture. The amount of all the precursors along with TEOS amount is listed in Table 1.

3. Characterization

Wide-angle X-ray diffraction (XRD) patterns were obtained using a PANalytical Empyrean multipurpose diffractometer with Cu-Kα radiation (λ_{avg}=1.5418 Å) at 35 kV and 30 mA at the Korea Basic Science Institute (KBSI) Daegu Center. Diffraction patterns were collected from 10 degrees to 90 degrees with a scan rate of 0.04 degrees/sec.

Atomic weight percentage of various metal ions present in different Ni-based multi-metal doped silica samples was analyzed by using an inductively coupled plasma optical emission spectrometer (ICP-AES, JobinYvonUltima 2C) with the wavelength to 395.254 nm at KBSI Seoul center. The final data was averaged after performing each experiment three times.

Transmission electron microscopy (TEM) images were obtained using a JEOL JEM-2010 microscope operating at 200 kV. Samples were prepared by sonicating a powder sample for 2 h to disperse it in acetone and then drop it onto a porous carbon-coated copper grid before measurement.

Field emission scanning electron microscopy (FE-SEM) images and elemental mapping images for Si and all metal species were obtained at a voltage of 15 kV using a JEOL JSM-4300F field emission scanning electron microscope equipped with an embedded energy dispersive system (EDS). Before the measurement, a powder sample was placed on a carbon film and coated with Pt.

Nitrogen adsorption isotherms were obtained using a Micromeritics 2420 analyzer. Samples were degassed at 623 K below 30 μmHg for about 5 h prior to analysis. The Brunauer-Emmet-Teller

(BET) specific surface area was evaluated by taking a part of adsorption isotherms in the relative pressure (P/P_0) range of 0.04-0.20. The total void volume (V_t) was obtained through the amount adsorbed at $0.99P/P_0$. The pore size distribution (PSD) curve was calculated from the adsorption isotherm using Barrett-Joyner-Halenda (BJH) method. The micropore volume (V_{micro}) was obtained through t-plot. The pore size (D_{BJH}) was taken as the maximum distribution value of PSD.

For the half-cell fabrication, the anode material was prepared using 70 wt% of each active material sample (NS, NCeS, NAS, and NCMAS) with polyvinylidene fluoride (PVDF) binder (15%) and super P carbon (15%) in N-methyl 2-pyrrolidone (NMP) solution. The above prepared slurry was well-ground and coated on copper foil using doctor blade technique, and then it was dried in a vacuum oven at 393 K for 12 h. After proper drying, it was cut into a circular disc and used as a working electrode (anode). The metallic Li foil and glassy fiber (Whatman GF/D) served as reference electrode and separator, respectively. 1 M $LiPF_6$ dissolved in mixed solvents of ethylene carbonate (EC) and diethyl carbonate (DEC) (1 : 1 volume ratio) was employed as electrolyte. For the full cell fabrication. the cathode material slurry was prepared using 70 wt% of $LiNi_{0.8}Mn_{0.1}Co_{0.1}O_2$ (LNMC) active material, 15 wt% of PVDF binder and 15 wt% of super P carbon in NMP solvent. The well mixed slurry was coated on aluminum foil and dried in a vacuum oven at 393 K for 12 h. After that, it was cut into circular shaped discs and used as a cathode material for full cell fabrication. For the full cell fabrication, except metallic Li foil, the above-mentioned same electrolyte and separator were utilized. The CR2032 coin type half-cell and full cell LIBs were fabricated in an argon-filled glove box. The galvanostatic charge-discharge (GCD) data was collected using WonaTech automatic battery cycling tester (WBCS3000) in the voltage range of 0.05-3 V (half-cell) and 1.8-4 V (full cell). The cyclic voltammetry (CV) measurement was at a scan rate of 0.2 mV s^{-1} between 0.001-3 V on Iviumstat electrochemical workstation. The EIS measurements were carried out using Iviumstat electrochemical workstation in the frequency range of 100 kHz to 10 mHz.

RESULTS AND DISCUSSION

Based on modified Stöber method [26], using ammonia base and CTAB surfactant, the Ni-based multi-metal-doped silica mesoporous sample was fabricated in water-ethanol mixed solvent media. A simple schematic representation of the synthesis pattern is shown in Scheme 1. A sol-gel reaction takes place to induce a slow hydrolysis of silica with Ni and other metal precursors. Sol to gel transformation during the ageing process at room temperature followed by solvothermal treatment at temperature 373 K helps proper growth of the metal-silica nanocrystals. Final calcination treatment results in the formation of well-defined Ni-multi-metal doped silica nanoflowers. Ammonia plays a critical role here by controlling the basicity of the media required for silica hydrolysis, as well as supporting the formation of morphology-oriented nanoparticles in aqueous ethanolic media [27].

Elemental composition of different metal ions have beewasn evaluated from ICP-AES elemental analysis and the data is shown in Table 2. Based on it, it is evident that NS sample has appreciable amount of Ni and Si species, whereas other samples NCeS, NAS, NCMAS, have also shown successful incorporation of all the respective metal species.

Wide angle powder X-ray diffraction analysis (XRD) was recorded to get information about the crystalline phase of the synthesized materials. Respective XRD data of the calcined samples are shown in Fig. 1(a)-(d). The sample NS with Ni/Si=0.83 ratio exhibits strong

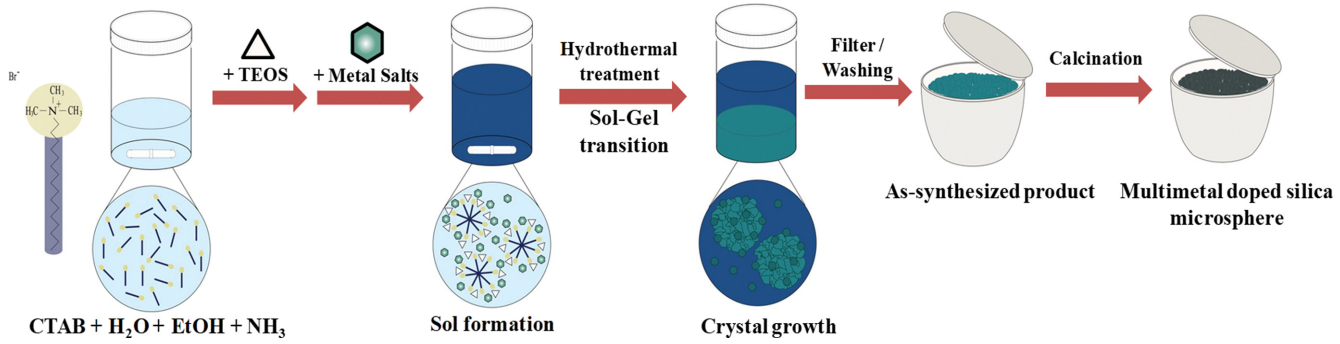

Scheme 1. Experimental procedure for synthesis of Ni-based multi-metal-doped silica microsphere in sol-gel hydrothermal method.

Table 2. Elemental composition of various Ni-based multi-metal doped mesoporous silica microsphere samples

Sample name	Elemental composition (wt%)						
	Ni	Si	O	Ce	Al	Mn	Co
NS	15.23	18.39	66.38	-	-	-	-
NCeS	13.45	16.37	69.29	0.89	-	-	-
NAS	13.06	16.27	66.14	-	4.53	-	-
NCMAS	11.02	17.21	63.99	-	2.89	2.62	2.26

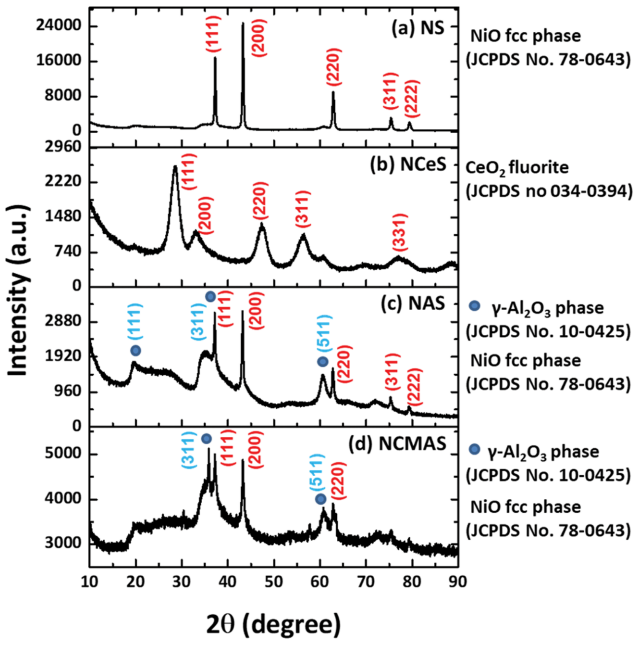

Fig. 1. Wide angle powder x-ray diffraction patterns of (a) NS, (b) NCeS, (c) NAS and (d) NCMAS samples. All peaks are indexed according to JCPDS file no.

diffraction peaks at 2θ=37.4, 43.4, 62.8 and 75.6 degrees (Fig. 1(a)) indicating a high crystallinity of the nickel-silica sample. Those peaks refer to the characteristic diffraction planes (111), (200), (220) and (311), respectively, for NiO face centered cubic phase matching with JCPDS file No. 78-0643 [27]. The lattice parameter a=4.17 Å and the average crystallite sizes obtained from Scherrer equation (i.e., $L=K\lambda/\beta\cos\theta$) are around 20-21 nm. A high concentration of Ni is responsible for the availability of NiO fcc crystalline phase in the NS sample. Next, the sample NCeS with doped Ce species shows predominant diffraction peaks at 2θ values= 28.4°, 32.6°, 47.5°, 56.3°, and 77.04° which are typical for face-centered cubic CeO_2 fluorite structure (JCPDS no 034-0394) corresponding to the crystal planes (111), (200), (220), (311), and (331), respectively (Fig. 1(b)) [28]. Absence of any significant diffraction peak indicates uniform distribution of all Ni species throughout silica matrix without leaving any isolated Ni species. This type of phenomenon is not rare in the literature [29]. Other sample NAS doped with Al species in Fig. 1(c) shows characteristic peaks at 2θ=37.4°, 43.2°, and 62.8° for cubic NiO phase along with some additional peaks at 2θ values of 19.7°, 36.9°, and 60.9°, indicating the presence of (111), (311) and (511) reflection planes, respectively, due to γ-Al_2O_3 crystalline phase (JCPDS PDF No. 10-0425) [30]. Fig. 1(d) represents the XRD pattern for NCMAS sample doped with multi-metal species like Co, Al, Mn onto Ni-silica structure. The material shows several peaks at 36.9°, 37.4°, 43.2°, 60.9°, and 62.8°, indicating the presence of mixed phase arising from cubic NiO and γ-Al_2O_3 crystalline phase. There is no significant peak due to other metal species Co and Mn. Hence, based on the XRD and ICP-AES analysis, it is quite evident that CTAB surfac-

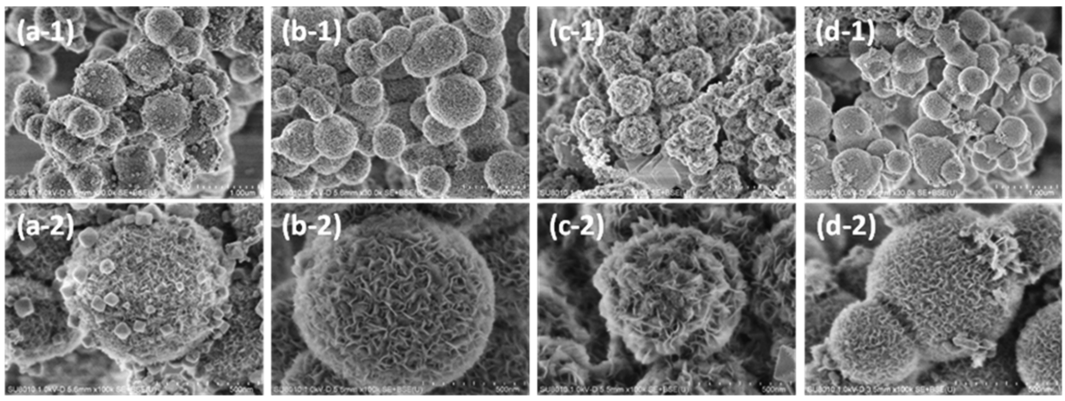

Fig. 2. FESEM images of (a) NS, (b) NCeS, (c) NAS and (d) NCMAS samples.

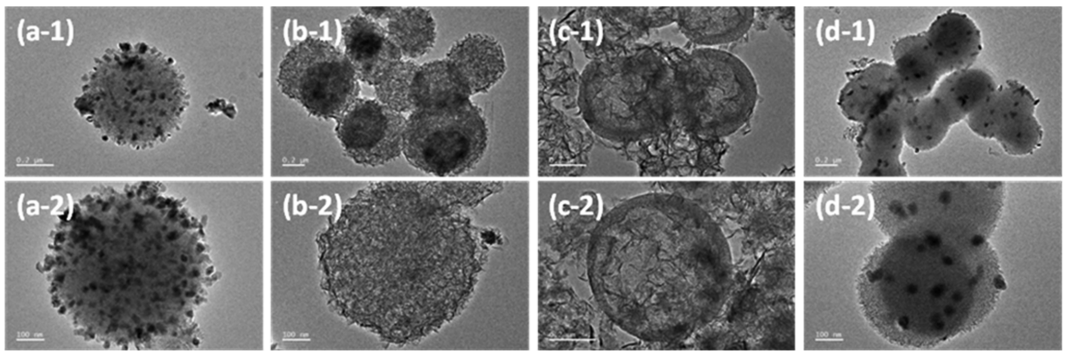

Fig. 3. TEM images of (a) NS, (b) NCeS, (c) NAS and (d) NCMAS samples.

tant and ammonia basic catalyst mediated sol-gel route has resulted in successful formation of nickel-silica platform incorporated with various metal species.

FE-SEM image of the as-prepared samples is recorded to know the structural morphology and particle size of the material. FE-SEM images of NS, NCeS, NAS, NCMAS samples are shown in Fig. 2(a)-(d). All the samples consist of 3-dimensional spherical particles of size 500-900 nm. Higher magnified images shows a beautiful flower-like morphology comprised of a number of petals throughout the whole specimen. From the FE-SEM images, it is evident that this nanoflower-like morphology is quite common for the Ni-silica based system synthesized in the present condition, irrespective of the nature of incorporated doping metal species.

TEM analysis was utilized to find the internal nanostructure of these multi-metal doped nickel-silica materials. Fig. 3(a)-(d) exhibits various TEM images of NS, NCeS, NAS and NCMAS samples. The images shown here indicate a spherical flower-like morphology of all the samples with fine-d petals distributed throughout the whole specimen. Moreover, wormhole like porosity of nanometer dimension is also observed in all the samples, as can be seen from the high-resolution image of the material.

Energy-dispersive spectrometry (EDS) mapping of all samples was recorded to justify the presence of different metal species in this material. The colored images displayed in Fig. 4(a) to (d) suggest that all the elements used in the synthesis gel are present in the respective samples. EDS mapping also confirms that each element is uniformly distributed throughout the silica framework.

Porous structure and surface area of these nickel based multi-metal doped-silica samples have been confirmed from the N_2 adsorption-desorption isotherm analysis of the material. N_2 sorption isotherms for NS, NCeS, NAS and NCMAS samples are shown in Fig. 5. The related physicochemical data evaluated from the sorption isotherm analysis is listed in Table 3. N_2 sorption isotherms exhibit typical type IV pattern according to IUPAC classification, which indicates mesoporous nature of the materials [29]. Moreover, the hysteresis loops and capillary condensation steps are observed in the relative pressure range P/P_0=0.42-0.90. This type of type IV isotherm along with hysteresis loop is one of the main characteristics of silica based mesoporous materials. Capillary evaporation is also observed to occur at a similar pressure range, indicating the true reversible nature of adsorption and desorption branches. Brunauer-Emmett-Teller (BET) surface area (S_{BET}) for

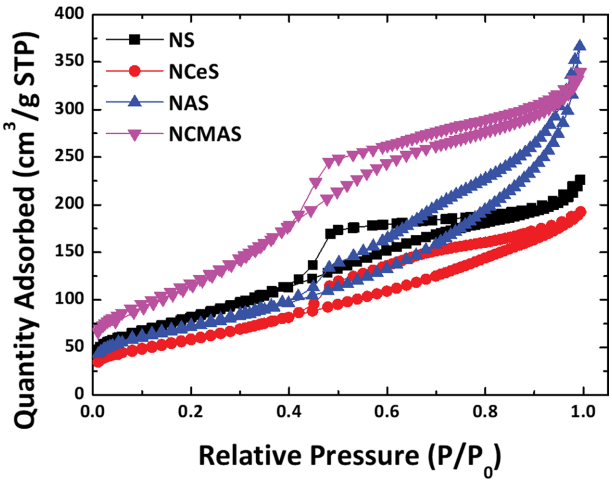

Fig. 5. Nitrogen adsorption-desorption isotherms for various Ni-based multi-metal doped mesoporous silica microsphere samples.

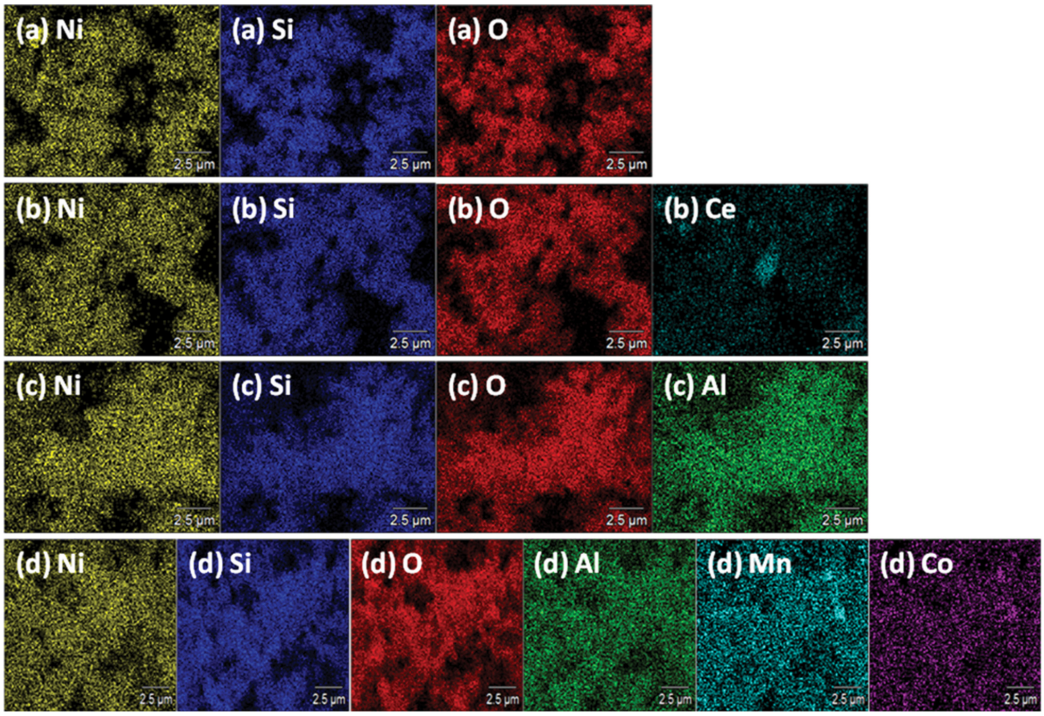

Fig. 4. EDS mapping images for different elements of (a) NS, (b) NCeS, (c) NAS, and (d) NCMAS samples.

Table 3. Physicochemical analysis of Ni-based multi-metal doped mesoporous silica microsphere samples*

Sample name	S_{BET} (m^2/g)	V_t (cm^3/g)	V_{micro} (cm^3/g)	D_{BJH} (nm)
NS	292	0.3497	0.0377	2.92
NCeS	211	0.2976	0.0270	2.82
NAS	255	0.5665	0.0064	3.14
NCMAS	405	0.5251	0.2328	3.00

*S_{BET}=BET specific surface area, V_t=total pore volume obtained at P/P_0=0.99, V_{micro}=*t*-plot micropore volume, D_{BJH}=pore width calculated at the maximum of PSD using BJH method.

the samples evaluated was in the range of 211-405 m^2g^{-1}, and the total pore volume (V_t) obtained at P/P_0=0.99 was from 0.30 to 0.56 cm^3g^{-1}, as listed in Table 3. Here, it is observed that, with decreasing Ni percentage in the silica-based materials, the surface area of the sample increases, whereas the increasing trend of surface order is not affected by the incorporation of doping metals. The sample NCMAS with lowest Ni content and maximum number of doping species shows highest surface area. The reason behind this is that a high percentage of Ni species in the framework (Ni/Si ratio= 0.64-0.83) somewhat disturbs the silica mesostructure, reducing its surface area, whereas doping of other metal ions in very small quantity (M/Si ratio=0.05-0.28) does not affect much the mesoporous silica framework. Decrease of surface area for mesoporous silica on incorporation of high metal content in silica framework has also been observed in the literature [30].

Pore size distribution (PSD) graphs were obtained by using Barrett-Joyner-Halenda (BJH) method (Fig. 6). All the samples NS, NCeS, NAS and NCMAS apparently exhibit a narrow pore size distribution. The pore diameters obtained corresponding to the peak maxima (D_{BJH}) are in the range of 2.82-3.14 nm as shown in Table 3. Although NS and NCMAS have shown narrow pore size distribution, indicating uniformity of pore size in the samples, somewhat broad peaks were obtained in case of NCeS and NAS. This indicates that the pore sizes of the two samples (NCeS and NAS) are not so uniform, having maxima near 3-4 nm and 7-8 nm. This type of broad pore size distribution for porous silica upon doping of metals is not very rare in literature [31]. The value indicates typical mesopore diameter observed for other samples in the literature. Thus, N_2 sorption analysis proves that in spite of high loading of Ni in the silica framework as well as significant doping of multi-metal ions, the porosity of the silica framework is retained with pore diameter being in the range of typical mesoporous material.

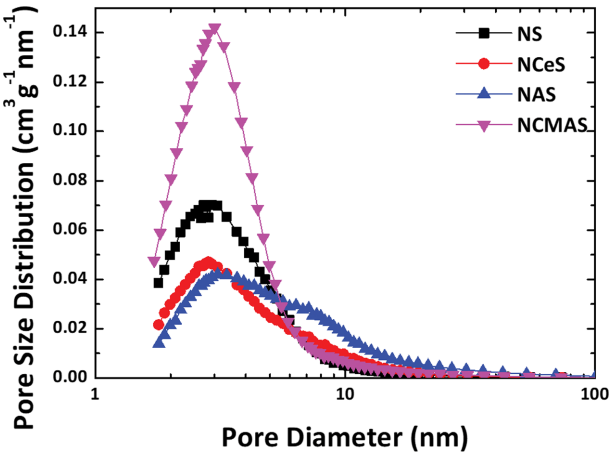

Fig. 6. Pore size distribution (PSD) plot for Ni-based multi-metal doped mesoporous silica microsphere samples based on BJH method.

Electrochemical performance of multi-metal doped nickel-silica was investigated based on cyclic voltammetry (CV) and galvanostatic charge-discharge (GCD) measurements of the samples. The CV curves for the NS and NCeS electrodes were measured between 0.001 and 3 V at a scan rate of 0.2 mV s^{-1} for initial three cycles and shown in Fig. 7(a). In CV curves, the lithium insertion/de-insertion process is similar for the both electrodes, which indicates the occurrence of similar oxidation/reduction process. For both electrodes, in initial cathodic sweep, the observed broad reduction peak between 0.3 to 1 V is due to the formation of solid electrolyte interface (SEI) film associated with the decomposition of electrolyte and the reduction of metal oxides such as SiO_2, CeO_2, and NiO to their metallic states [32,33]. For the subsequent cycles, it was shifted to higher potential side. During the anodic scan, multiple oxidation peaks were observed, indicating that the extraction of Li^+ takes place in several ways due to the electrode composed of multi metal oxides. In NS electrode, three reduction peaks were observed at ~0.45, 1.49, and 2.18 V. The small oxidation peak at 0.45 V is attributed to the lithiation of Li_xSi [34]. Another two reduction peaks at 1.49 and 2.18 V correspond to the decomposition of Li_2O and oxidation of NiO [35,36]. Whereas, four oxidations peaks at ~0.47, 1.45, 2.1, and 2.43 V were observed for the NCeS electrode in initial anodic sweep. The oxidation peaks at 0.47 and 1.45 V are attributed to the lithiation of Li_xSi and oxidation of Ce to CeO_2, respectively [34,35]. The peaks remaining at 2.1 and 2.43 V are associated with the decomposition of Li_2O and oxidation of NiO [36,37]. For the subsequent cycles, the peak intensity and integrated area of the electrode is overlapped, indicating the partial reversibility of the electrode material.

For the subsequent cycles, the peak intensity and integrated area of the NCeS electrode are overlapped compared to the other two electrodes, indicating that partial reversibility is possible for NCeS electrode only.

The GCD curves and cycling performance of the NS and NCeS electrodes were measured at a current density of 100 mA g^{-1} between 0.05 and 3 V. The GCD profiles for the NS and NCeS electrodes are shown in Fig. 7(b), and the corresponding cycling performance for all the electrodes is shown in Fig. 7(c). Both electrodes exhibit a voltage plateau between 0.4 and 1 V during the initial

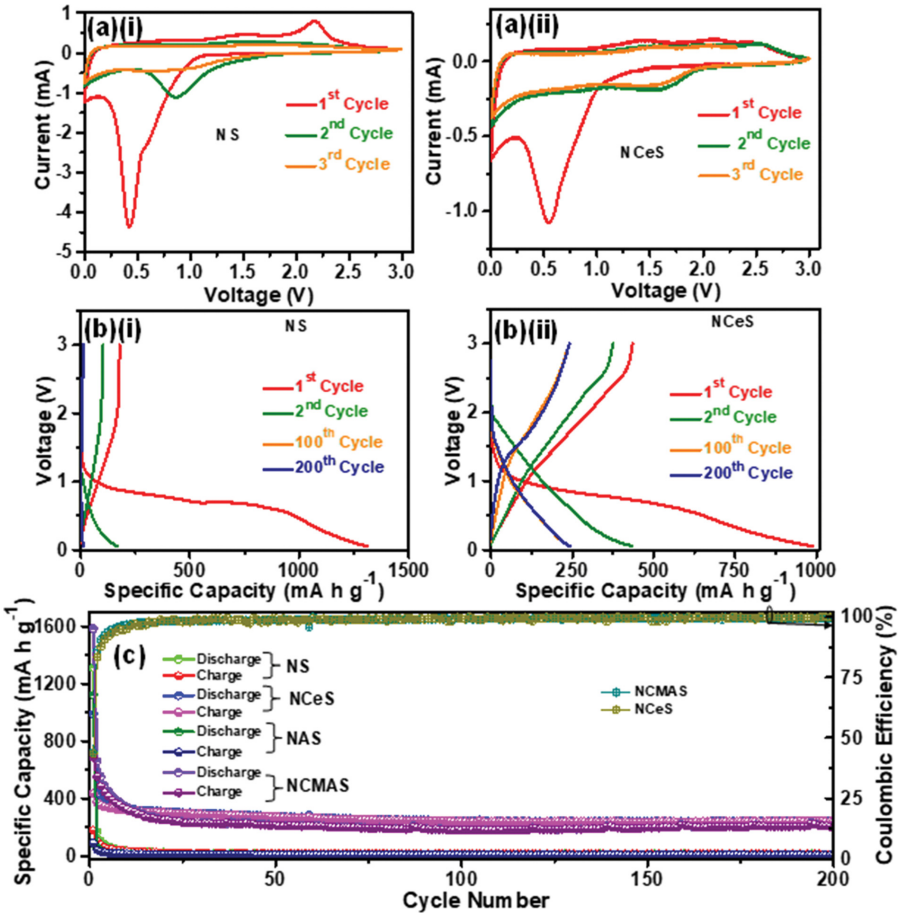

Fig. 7. (a) CV curves of the NS and NCeS electrodes at scan rate of 0.2 mV s^{-1}. (b) GCD curves of the NS and NCeS electrodes at 100 mA g^{-1}. (c) Cycling performance of the NS, NCeS, NAS, and NCMAS electrodes at 100 mA g^{-1}.

cathodic scan, which is well in accordance with the measured CV results. The initial charge/discharge capacity was found to be 1,313/178, 990/436, 1,122/234, and 1,585/689 mA h g^{-1} for the NS, NCeS, NAS, and NCMAS electrodes, respectively. The obtained Coulombic efficiency (CE) values of the NS, NCeS, NAS and NCMAS electrodes are about 14, 44, 21, and 43%, respectively. The obtained low CE of the electrodes is mainly attributed to the formation SEI film on the surface of the electrode material and the decomposition of the electrolyte during the first cycle [38]. Comparatively, the NCeS and NCMAS electrodes exhibited higher initial CE than the other two electrodes, abruptly improving 86 and 83% for the second cycle. After 200 cycles, the NS, NCeS, NAS, and NCMAS electrodes stored reversible capacity of 14, 243, 7, and 205 mA h g^{-1}, respectively. Among all the electrodes, the NCeS electrode stored high discharge capacity with the CE of 99.6%. The rate performance was measured for the NCeS electrode, as shown in Fig. 8(a). The delivered discharge capacity is about 292, 225, 185, and 158 mA h g^{-1} at 200, 400, 600, and 800 mA g^{-1}, respectively. The discharge capacity of 231 mA h g^{-1} with CE of 99.1% remained when reversed back to its initial current density of 200 mA g^{-1}. EIS is the best tool to find the kinetic transport properties of the electrode materials. The EIS measurements were carried out on fresh cells for the NS, NCeS, NAS, and NCMAS electrodes and shown in Fig. 8(b). From Fig. 8(b), all the electrodes exhibit a semicircle arc in the high frequency region and the inclined line in the low frequency region. The semicircle in the high frequency region indicates the charge transfer resistance (R_{ct}) and the inclined line in the low frequency region corresponds to the Warburg impedance. The diameters for the NCeS and NCMAS electrodes are smaller than that of the NS and NAS electrodes, suggesting the lower resistance for the NCeS and NCMAS electrodes. And the NCeS electrode exhibits lower resistance than the NCMAS, implying that the NCeS electrode shows higher electrical conductivity among all the electrodes. The higher electrical conductivity of electrode materials can boost the migration of ions, which leads to the enhancement of their cycling performance.

Finally, the full cell was also fabricated using the LNMC as a cathode and NCeS as an anode by maintaining the mass loading of 5 : 1. Our schematic strategy for the fabrication of full cell is shown in Fig. 8(c). Fig. 8(d) shows the selected GCD curves and Fig. 8(e) shows the cycling performance for the NCeS//LNMC full cell at a current density of 100 mA g^{-1}. The charge/discharge capacity of 166/41 mA h g^{-1} was obtained for the first cycle. The discharge capacity of 13.6 mA h g^{-1} remained after 50 cycles. The cycling performance of the full cell not only depends on an anode material but also relies on the morphology and structural stability

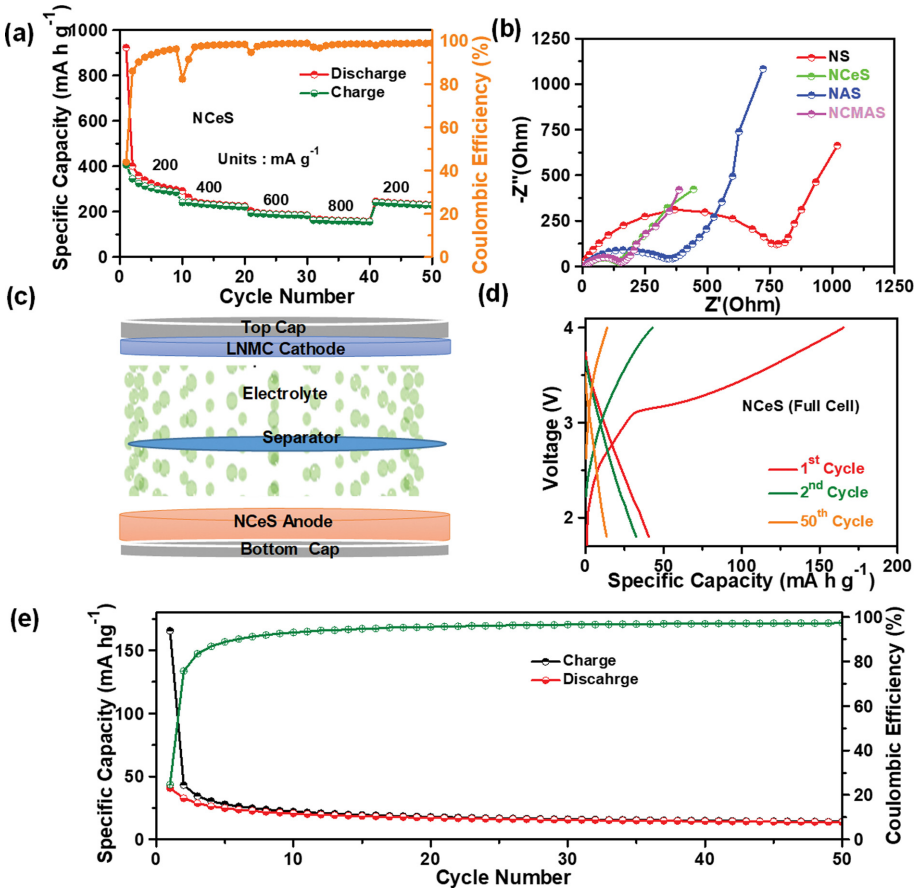

Fig. 8. (a) Rate performance of NCeS electrode at different current densities. (b) EIS plots of all the electrodes. (c) Schematic strategy for the fabrication of CR2032 coin type full cell. (d) GCD curves and (e) cycling performance of NCeS//LNMC full cell at a current density of 100 mA g^{-1}.

of cathode materials. In this work, the particle size of the commercially employed LNMC was about 500 nm. The large particle size of the cathode material may be the possible reason for the huge capacity fading of the full cell upon the continuous cycling.

Among the all electrodes, the NCeS demonstrated good reversibility and rate performance with high Coulombic efficiency among all the electrodes; this may be due to high electrical conductivity of the electrode. The presence of Ce and Ni elements may allow good conductivity throughout the electrode material. The high electrical conductivity can allow the fast diffusion of Li ions/electrons, resulting in an improvement of their electrochemical performance. Apart from that, porous 3D structure not only releases the strain induced by volume variation during the cycling process and also provides good contact between the electrode/electrolyte interfaces. As a consequence, enhanced electrochemical performance for the NCeS electrode is observed.

CONCLUSIONS

Mesoporous Ni-based silica nanoflowers which have been employed as an anode material for rechargeable Li-ion battery application were fabricated in a simple sol-gel hydrothermal method using a CTAB surfactant and ammonia basic catalyst in water-ethanol mixed solvent media. The material upon doping with several metals like Ce, Al and a combined doping of Co, Mn, Al species together was investigated as an electrode preparation for LiBs. In particular, NCeS electrode exhibited excellent cycling performance with improved CE and good rate performance compared to the other samples. Unique 3D flower-like hierarchical features, typical mesoporous nanostructures, and excellent conductivity between Ce and Ni species over the silica framework, all these together facilitate improved electrochemical performance for NCeS electrode. This systematic investigation can be a guiding effort for the development of other mesoporous silica-based anode materials.

ACKNOWLEDGEMENTS

E.-B. Cho acknowledges support of the National Research Foundation of Korea (NRF-2020R1A2C1015117). N. Pal conveys gratitude to TEQIP-III, JNTUH, Hyderabad for providing her the funding support in this work (letter no. JNTUH/TEQIP/CRS/2019/Chemistry/03).

REFERENCES

1. P. A. Owusu and S. Asumadu-Sarkodie, *Cogent Engineer.*, **3**, 1167990

(2016).
2. P. Kruger, *Alternative energy resources: The quest for sustainable energy*, Wiley Publications (2006).
3. A. Sternberg and A. Bardow, *Energy Environ. Sci.*, **8**, 389 (2015).
4. D. Nathan, O. N. Nzewi, K. C. Onuora and A. O. Abioye, *Quest J. Electronics Commun. Eng. Res.*, **1**(1), 01 (2013).
5. S. Ge, Y. Leng, T. Liu, R. S. Longchamps, X.-G. Yang, Y. Gao, D. Wang, D. Wang and C.-Y. Wang, *Sci. Adv.*, **6**, eaay7633 (2020).
6. U. Eberle and R. Von Helmolt, *Energy Environ. Sci.*, **3**, 689 (2010).
7. D. Larcher and J.-M. Tarascon, *Nat. Chem.*, **7**, 19 (2015).
8. J. Cabana, L. Monconduit, D. Larcher and M. R. Palacín, *Adv. Mater.*, **22**, E170 (2010).
9. G. Gao, S. Lu, B. Dong, Y. Xiang, K. Xi and S. Ding, *J. Mater. Chem.*, **4**, 6264 (2016).
10. Y. Zhao, X. Li, B. Yan, D. Xiong, D. Li, S. Lawes and X. Sun, *Adv. Energy Mater.*, **6**, 1502175 (2016).
11. P. M. Ette, A. Chithambararaj, A. S. Prakash and K. Ramesha, *ACS Appl. Mater. Interfaces*, **12**, 11511 (2020).
12. S. Balamurugan, N. Naresh, I. Prakash and N. Satyanarayan, *Appl. Surf. Sci.*, **535**, 147677 (2021).
13. J.-Y. Li, Q. Xu, G. Li, Y.-X. Yin, L.-J. Wan and Y.-G. Guo, *Mater. Chem. Front.*, **1**, 1691 (2017).
14. P. Li, G. Zhao, X. Zheng, X. Xu, C. Yao, W. Sun and S. X. Dou, *Energy Storage Mater.*, **15**, 422 (2018).
15. A. Mishra, A. Mehta, S. Basu, S. J. Malodeb, Nagaraj P. Shetti, Shyam S. Shukla, M. N. Nadagouda and T. M. Aminabhavi, *Mater. Sci. Energy Technol.*, **1**(2), 182 (2018).
16. N. Nitta, F. Wu, J. T. Lee and G. Yushin, *Mater. Today*, **18**(5), 252 (2015).
17. J. Harris, R. Silk, M. Smith, Y. Dong, W.-T. Chen and G. I. N. Waterhouse, *ACS Omega*, **5**, 18919 (2020).
18. S. Sun, X. Zhang, Y. Sun, S. Yang, X. Song and Z. Yang, *Phys. Chem. Chem. Phys.*, **15**, 10904 (2013).
19. M. Negahdary and H. Heli, *Recent Patents on Nanotechnol.*, **12**, 22 (2018).
20. T. Tao, Y. Chen, Y. Chen, D. S. Fox, H. Zhang, M. Zhou, M. Raveggi, A. J. Barlow and A. M. Glushenkov, *ChemPlusChem*, **82**, 295 (2017).
21. P. Shende, P. Kasture and R. S. Gaud, *Artif. Cells Nanomed. Biotechnol.*, **46**(S1), S413 (2018).
22. L. Li, M. Ye, Y. Ding, D. Xie, D. Yu, Y. Hu, H.-Y. Chen and S. Peng, *J. Alloys Compounds*, **812**, 152099 (2020).
23. Z. Tariq, S. U. Rehman, J. Zhang, F. K. Butt, X. Zhang, B. Cheng, S. Zahra and C. Li, *Mater. Sci. Semicond. Process.*, **123**, 105549 (2021).
24. S. Liu, B. Shen, Y. Niu and M. Xu, *J. Colloid Interface Sci.*, **488**, 20 (2017).
25. S.-W. Kim, D.-H. Seo, H. Gwon, J. Kim and K. Kang, *Adv. Mater.*, **22**, 5260 (2010).
26. W. Stöber and A. Fink, *J. Colloid Interface Sci.*, **26**, 62 (1968).
27. N. Pal, S. Im, E.-B. Cho, H. Kim and J. Park, *J. Ind. Eng. Chem.*, **81**, 99 (2020).
28. N. Pal, E.-B. Cho and D. Kim, *RSC Adv.*, **4**, 9213 (2014).
29. A. K. Patra, A. Dutta and A. Bhaumik, *J. Hazard. Mater.*, **201-202**, 170 (2012).
30. S. Hao, Z. Wang and L. Chen, *Mater. Des.*, **111**, 616 (2016).
31. S. Zhou, H. Zhao, D. Ma, S. Miao, M. Cheng and X. Bao, *Z. Phys. Chem.*, **219**, 949 (2005).
32. W. Derafa, F. Paloukis, B. Mewafy, W. Baaziz, O. Ersen, C. Petit, G. Corbel and S. Zafeiatos, *RSC Adv.*, **8**, 40712 (2018).
33. D. Xie, W. Yuan, Z. Dong, Q. Su, J. Zhang and G. Du, *Electrochim. Acta*, **92**, 87 (2013).
34. Z. Favors, W. Wang, H. H. Bay, A. George, M. Ozkan and C. S. Ozkan, *Sci. Rep.*, **4**(1), 1 (2014).
35. M. Ma, H. Wang, S. Liang, S. Guo, Y. Zhang and X. Du, *Electrochim. Acta*, **256**, 110 (2017).
36. B. Varghese, M. Reddy, Z. Yanwu, C. S. Lit, T. C. Hoong, G. Subba Rao, B. Chowdari, A. T. S. Wee, C. T. Lim and C.-H. Sow, *Chem. Mater.*, **20**(10), 3360 (2008).
37. X. Huang, J. Tu, B. Zhang, C. Zhang, Y. Li, Y. Yuan and H. Wu, *J. Power Sources*, **161**(1), 541 (2006).
38. Y. Kang, Y.-H. Zhang, Q. Shi, H. Shi, D. Xue and F.-N. Shi, *J. Colloid Interface Sci.*, **585**, 705 (2021).